ADVANCED FUNCTIONAL MATERIALS
www.afm-journal.de

Self-Propelled Morphing Matter for Small-Scale Swimming Soft Robots

Chuqi Huang, Natalie P. Pinchin, Chia-Heng Lin, Irving Hafed Tejedor, Matthew Gene Scarfo, Hamed Shahsavan, and Abdon Pena-Francesch**

Aquatic insects have developed versatile locomotion mechanisms that have served as a source of inspiration for decades in the development of small-scale swimming robots. However, despite recent advances in the field, efficient, untethered, and integrated powering, actuation, and control of small-scale robots remains a challenge due to the out-of-equilibrium and dissipative nature of the driving physical and chemical phenomena. Here, we have designed small-scale, bioinspired aquatic locomotors with programmable deterministic trajectories that integrate self-propelled chemical motors and photoresponsive shape-morphing structures. A Marangoni motor system is developed integrating structural protein networks that self-regulate the release of chemical fuel with photochemical liquid crystal network (LCN) actuators that change their shape and deform in and out of the surface of water. While the diffusion of fuel from the motor system regulates the propulsion, the dissipative photochemical deformation of LCNs provides locomotors with control over the directionality of motion at the air-water interface. This approach gives access to five different but interchangeable modes of locomotion within a single swimming robot via morphing of the soft structure. The proposed design, which mimics the mechanisms of surface gliding and posture change of semiaquatic insects such as water treaders, offers solutions for autonomous swimming soft robots via untethered and orthogonal power and control.

1. Introduction

The development of untethered small-scale robots (ranging from a few nanometers to millimeters) has been the subject of growing research over the past two decades. The utility of small-scale robots in confined and flooded environments, such as inside the human body, holds significant promise in various fields, including medicine, where they could be used for targeted and non-invasive medical procedures, as well as in environmental monitoring and sensing applications.[1–3] Such robots can be remotely powered and controlled without requiring cables, pumps, or other external tethers via different actuation mechanisms[4,5] using magnetic fields,[6,7] light,[8,9] acoustic fields,[10,11] electric fields,[12] and chemical energy.[13–15] While these actuation methods present advantages in the miniaturization of robots (as they rely on off-board power generation), they still present limitations in their control to realize multiple robotic functions. For

C. Huang, C.-H. Lin, A. Pena-Francesch
Department of Materials Science and Engineering
University of Michigan
Ann Arbor, MI 48109, USA
E-mail: abdon@umich.edu

N. P. Pinchin, I. H. Tejedor, M. G. Scarfo, H. Shahsavan
Department of Chemical Engineering
University of Waterloo
Waterloo, ON N2L 3G1, Canada
E-mail: hshahsav@uwaterloo.ca

The ORCID identification number(s) for the author(s) of this article can be found under https://doi.org/10.1002/adfm.202413129

DOI: 10.1002/adfm.202413129

H. Shahsavan
Center for Bioengineering and Biotechnology
University of Waterloo
Waterloo, ON N2L 3G1, Canada

H. Shahsavan
Waterloo Institute for Nano Technology
University of Waterloo
Waterloo, ON N2L 3G1, Canada

A. Pena-Francesch
Department of Chemical Engineering
University of Michigan
Ann Arbor, MI 48109, USA

A. Pena-Francesch
Macromolecular Science and Engineering
University of Michigan
Ann Arbor, MI 48109, USA

A. Pena-Francesch
Robotics Institute
University of Michigan
Ann Arbor, MI 48109, USA

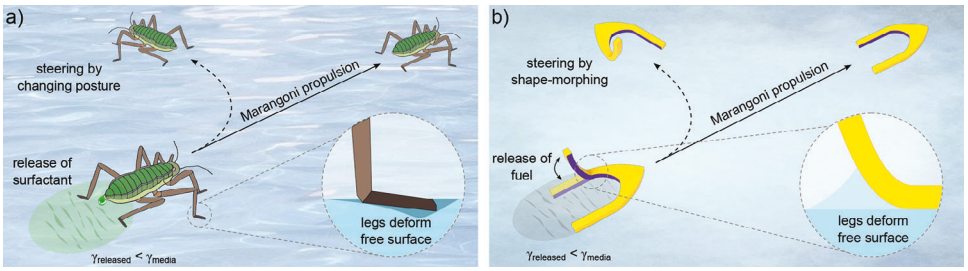

Figure 1. Bioinspired design of a self-propelled shape-morphing swimming robot. a) A water treader swims by secreting a biosurfactant to generate Marangoni propulsive force while adjusting their posture to steer and change trajectory. b) A bioinspired soft robot integrates surface tension motors with photochemical morphing structure to mimic the swimming mechanism of water treaders by releasing chemical fuel for propulsion, while morphing their structure for steering respectively.

example, many magnetic microrobots use magnetic fields for propulsion only (using rotating fields and magnetic torque to propel a helical structure forward).[6,16,17] Other stimuli like electric fields and chemical gradients can be used to induce electrophoresis or chemotaxis to generate motion,[18,19] and light can be used to induce underwater locomotion via photothermal heating or photo-responsive bending or contraction.[8] Each of these stimuli is typically used to individually induce one single type of action, with limited capabilities to perform different functions and to simultaneously address multiple agents. Combining different stimuli, one can integrate different responses in the robot design and leverage different actuation mechanisms to decouple functions. For example, recent works have used acoustic fields or chemical energy for propulsion while using external magnetic fields and torque to steer the microrobot, thus decoupling propulsion and direction control.[20,21] However, this approach adds significant efficiency penalties, loss of autonomy, and complexity, as it requires two active energy delivery and actuation systems to provide decoupled stimuli simultaneously.

Biology has developed many versatile mechanisms to generate complex locomotion in organisms at small length scales without the need for decoupled external stimuli. For example, shape-morphing is a prevalent approach observed in nature to alter the locomotion gait of small organisms.[22] Amoebas are unicellular organisms that move by altering their shape extending and retracting pseudopods (fingerlike protrusions of cytoplasm).[23] Nematodes are small roundworms that exhibit thrashing motion from contracting their longitudinal muscles, causing them to wriggle forward through soil, biological tissue, and other complex media.[24] This morphing approach has proven very useful in semiaquatic insects capable of moving on the surface of water. Small water-walking insects leverage the synergy between curvature forces and body-fluid interactions in changing their shape, posture, gaits, or leg movement to manipulate the free surface of water and induce locomotion. These semiaquatic insects are comparable in size to the capillary length and can be characterized by small Bond numbers (ratio of buoyancy to curvature $Bo << 1$), and Weber numbers (ratio of inertial forces to curvature $We < 1$). Such small Bo and We indicate that surface tension is dominant over gravitational forces and forces exerted by insect legs do not penetrate the free surface of water, respectively.[22,25] For example, *Pyrrhalta nymphaeae* larvae arch their backs to deform the free surface of the water and generate capillary forces to climb menisci.[26] *Gerridae* water striders have waxy fibrous legs that allow them to walk, row, and jump on water performing specific leg motions without breaking the surface tension.[27] Particularly relevant to this work, water treaders *Microvelia* and *Mesovelia* move on water through a combination of Marangoni propulsion and intricate deformation of the free surface.[28] These insects secrete surfactant molecules from their anus that reduce the local surface tension behind them, thus propelling them forward and gliding on water toward a higher surface tension. Concurrently, the insects move their legs in specific postures to deform the free water surface and morph the surface tension gradient, thus steering and adjusting their gliding trajectory.[22,29] This locomotion strategy provides coupled means of propulsion and steering through the combination of chemical (release of surfactant) and mechanical (bending of water surface) phenomena (**Figure 1a**), which present new design opportunities for autonomous semiaquatic robots.

While insects and small organisms have inspired the design of diverse locomotion mechanisms for many small-scale robots (including robotic inchworms,[30] ant swarms,[31] water striders,[32] bacteria,[33] etc.), most synthetic bioinspired locomotion mechanisms rely on only one approach and do not capture the delicate interplay between propulsion and shape-morphing found in biological swimmers. For example, most synthetic morphing swimmers typically rely on undulating stimulation to sustain their locomotion.[8,34] On the other hand, self-propelled swimmers are typically composed of passive structures with the capacity to store chemical fuel or to harvest from the environment with little control over propulsion and trajectories. More specifically, past efforts to design surface swimming robots inspired by water treaders and using Marangoni propulsion had significant shortcomings that limited their practical applications, as they often lacked control (random motion), efficiency (large volumes of fuel required), autonomy (shortlived locomotion requiring constant fuel supply), or required external accessories and mechatronic components (thus increasing size, weight, and complexity).[21,35,36] Therefore, designing a locomotion strategy that interlinks both propulsion and morphing in untethered small-scale robots will provide an adaptive, autonomous feedback mechanism to control the bioinspired robot trajectories and better recapitulate insect locomotive functions and overall performance.

Morphing swimmers in nature rely on the undulation of their geometry either to create propulsive forces or to give directionality to their movement. For example, *Hexabranchus sanguineus*

(Spanish dancer sea slug) uses stroke-relaxation cycles of its trunk to create propulsive forces and traveling waves on its peripheral membranes to fine-tune such forces.[37] Creating such undulating morphing in artificial swimmers has been achieved in various stimuli-responsive soft materials, such as liquid crystal networks (LCN).[8,34] LCNs are crosslinked polymers with anisotropic liquid crystalline molecules, i.e., mesogens, pending from or inside their backbone. Shape-change programming of LCNs can be readily obtained and tuned by control of alignment and distortion of mesogens' order in response to external stimuli. The major drawback of using LCNs as morphing swimmers is their dependence on light or heat for shape change. The order-to-disorder transition of LCN can be introduced directly by hot water or indirectly through light (*photothermal* heating). As such, photothermal mechanisms, where LCNs contain dopants that convert light into heat, have been commonly used for the design of morphing swimmers submerged in water[8] or on the air-water interface.[38,39] However, consecutive and fast heating and cooling of LCNs in water is impractical for swimming due to a low efficiency derived from large heat dissipation in water, low stroke frequency, and the need for high-intensity light stimuli to achieve dynamic shape morphing.[8] One could circumvent inefficient photothermal aquatic actuation through photochemical mechanisms. This strategy has been elegantly utilized for the design of artificial swimming jellyfish and aquatic polyps that grasp and release objects inside water.[34,40] Photochemical LCNs, typically, contain azobenzene derivatives as photo-switches to achieve deformation. The photoisomerization of azobenzene from the extended *trans* isomer to the bent *cis* isomer reduces the order of the liquid crystals, which can then be translated into macroscopic shape change. While photothermal LCNs require constant exposure to light to maintain their deformed shape, photochemical LCNs will retain their shape for a length of time proportional to the lifetime of the meta-stable *cis* isomer. This lifetime can be tuned by modifying the structure of the azobenzene compound used.[41] The *cis-to-trans* transition can be triggered using light, with wavelengths different than that of *trans-to-cis* excitation, or heat, through thermal back-relaxation. This allows for the actuation and relaxation of photochemical LCNs on demand, without the use of continuous illumination, positively impacting the overall efficiency of actuation.

Here, we propose the integration of chemical motors and photochemical shape-morphing structures into a programmable soft matter system for untethered propulsion and control of a small-scale robotic swimmer. We leverage recent breakthroughs in the design of Marangoni motors using structural protein networks with adaptive dynamic porosity to efficiently self-regulate the release of fuel and in the design of photochemical LCNs to bend and deform the air-water interface. Previously reported LCN soft robotic swimmers at the air-water interface rely on non-reciprocal photothermal[38,39] or photochemical[42,43] deformation of their soft bodies for propulsion, meaning that the mechanism controlling locomotion and steering are intrinsically coupled.[44] However, the hybrid locomotion mechanism herein involves Marangoni propulsion forces that are generated through fuel release, while simultaneously photochemical deformations of the LCN soft body control the trajectory by morphing the legs of the swimmer upward into the air or downward into the water. The design of photochemical responsive LCN formulations proved to be crucial for creating lasting and stable spatiotemporally anisotropic geometries of the swimmers and the directional diffusion of fuel from protein motors, a key advantage over previous photothermal systems. In the absence of any external magnetic field, such a design endowed single swimmers with five different modes of locomotion, which were dictated by their instantaneous geometry. We demonstrate the proposed hybrid locomotion mechanism in a proof-of-concept self-propelled morphing swimmer capable of passively and actively transitioning between locomotion modes.

2. Results

2.1. Concept and Design Approach

Inspired by the surface locomotion mechanism of *Velia* semi-aquatic insects, we propose here a hybrid swimmer design consisting of a modular motor for propulsion and a shape-morphing chassis structure for steering (Figure 1b). First, we design a surface tension self-powered motor that fulfills the following requirements: i) the motor system must have high efficiency so small amounts of chemical fuel can generate large propulsive forces for prolonged times, ii) the motor must be modular and compatible with other substrate materials so it can be applied to the shape-morphing chassis in a variety of configurations, iii) the motor system must have significant mobility lifetime to enable functionality, and iv) must be non-toxic. Second, we design a shape-morphing photochemical LCN chassis to modulate and deform the air-water interface that must: a) be tunable and capable of programmable, reversible, on-demand bending and relaxation, b) have large actuation strain to effectively modulate the capillary line in water, and c) have lasting and stable deformation states without continued exposure to high-intensity external stimuli (shape is retained when light is off). Below, we sequentially describe the design strategies for responsive soft matter engineering for surface tension protein-based motors and a photochemical LCN chassis. We then integrate them into functional self-propelled shape-morphing swimming robots with multiple locomotion modes and transition states.

2.2. Self-Propelled Protein Motor System

To develop a modular propulsion mechanism for our soft millirobotic system, we designed a protein-based self-propelled chemical motor, consisting of squid sucker ring teeth (SRT) proteins as an active porous biopolymer matrix, hexafluoroisopropanol (HFIP) as chemical fuel, and a dye (purple color) for better visualization (**Figure 2a**). SRT is a family of structural proteins extracted from squid suction cups that self-assemble into semicrystalline hydrogen-bonding-stabilized protein networks, forming solid films rich in β-sheet nanostructures.[45,46] SRT proteins have been recently explored as a modular chemical motor for small-scale mobile robots,[21,47,48] as well as in soft robotic actuators.[49,50] HFIP is a volatile solvent with low surface tension that disrupts hydrogen bonding and is commonly used to solubilize proteins.[51] An ideal chemical fuel for Marangoni propulsion

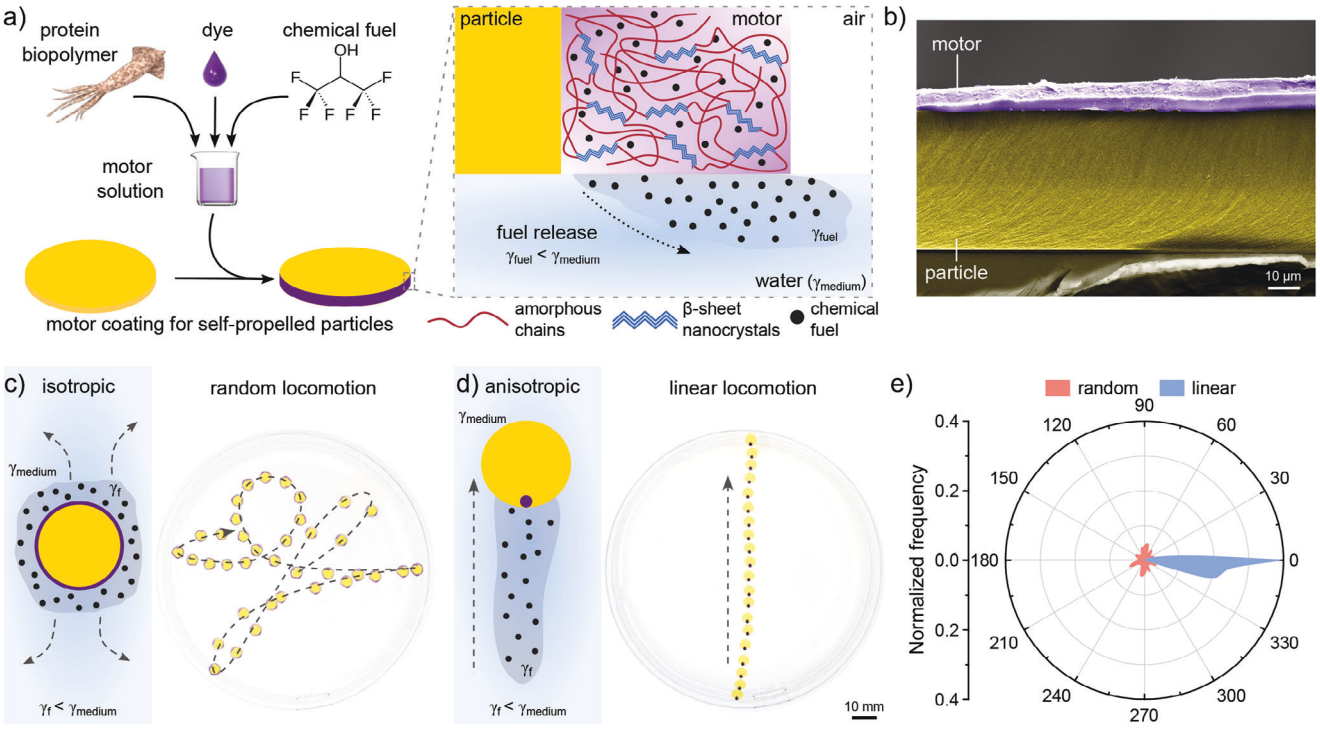

Figure 2. Protein motors. a) Preparation and application of protein-based motor coating composed of SRT proteins as motor matrix, HFIP as chemical fuel, and dye for visualization; fuel release from protein matrix into surrounding water medium, leading to surface tension gradients. b) SEM image of the particle-motor interface, with the liquid crystal network particle in yellow and the protein motor in purple. c) Isotropic and d) anisotropic motor coating generating surface tension gradients resulting in random and linear trajectories, respectively. e) Direction of locomotion in random and linear trajectories relative to particle orientation.

should not only have a low surface tension, but also be volatile so fuel is not accumulated in the swimming medium (reducing the global surface tension of the medium over time). Many organic solvents fall within these requirements, such as ethanol (γ = 33 mN m^{-1}), methanol (22.1 mN m^{-1}), isopropanol (22.3 mN m^{-1}), acetone (23.7 mN m^{-1}), hexane (18.4 mN m^{-1}), etc. However, since the swimmer particle will be moving through the medium, the released fuel will be diluted over the traveled volume. Therefore, the fuel should ideally be able to greatly reduce the local surface tension at very low concentrations. HFIP not only has very low nominal surface tension (γ = 14.7 mN m^{-1}), but also can greatly reduce the surface tension in water at very small concentrations. In a previous study, low surface tension solvents were screened as fuel candidates for their capacity to generate surface tension gradients as a function of their concentration in water.[47] Among the analyzed fuel candidates, HFIP exhibited the best performance with the largest gradients at small concentrations.[47] The SRT/HFIP solution can be conformally coated and applied onto a wide variety of substrate materials. When a coated particle was exposed to water, the entrapped HFIP inside the coated area slowly diffused out of the protein motor, thus locally decreasing the surface tension around the object. The fuel release mechanism was verified by Fourier transform infrared (FTIR) spectroscopy. The diffusion of fuel out of the protein motor matrix was observed in the disappearance of characteristic HFIP absorption bands in the 1000–1300 cm^{-1} region after exposure to water (Figure S1a, Supporting Information). While entrapped HFIP prevents the formation of β-sheet nanocrystals in the protein matrix, its release allows SRT proteins to self-assemble and form domains rich with β-sheet nanocrystals. We confirmed this through the shift of the amide I band from 1640 to 1633 cm^{-1} (Figure S1b, Supporting Information). The formation of β-sheet nanocrystals plays a critical role in regulating the internal diffusion of entrapped fuel within the protein matrix. As a result, residual fuel experiences prolonged diffusion, thereby extending the continuous motor lifetime, surpassing other fuel-motor materials system combinations.[47] The presence of amide I, amide II, and amide A bands (characteristic of proteins at 1580–1720 cm^{-1}, 1470–1570 cm^{-1}, and 3000–3600 cm^{-1}, respectively) observed in motor-coated disk particles confirmed good adhesion and stability of the motor films (Figure S2, Supporting Information). Scanning electron microscopy (SEM) images further confirm the good stability and adhesion between particles and motor coating (Figure 2b; Figure S3, Supporting Information).

Since the protein motor system can be applied as a coating to arbitrary materials and geometries, it can be applied as a modular motor to inactive particles in predefined locations to generate anisotropy in surface tension gradients. For example, a disc particle that has been homogeneously coated with the protein motor material system (violet dye) is expected to generate a uniform isotropic surface tension gradient caused by the homogeneous release of fuel in all directions (and consequently, no directional preference in its motion) (Figure 2c; Movie S1, Supporting Information). However, small vibrations and flow fluctuations can randomly disrupt the isotropic surface tension gradient,

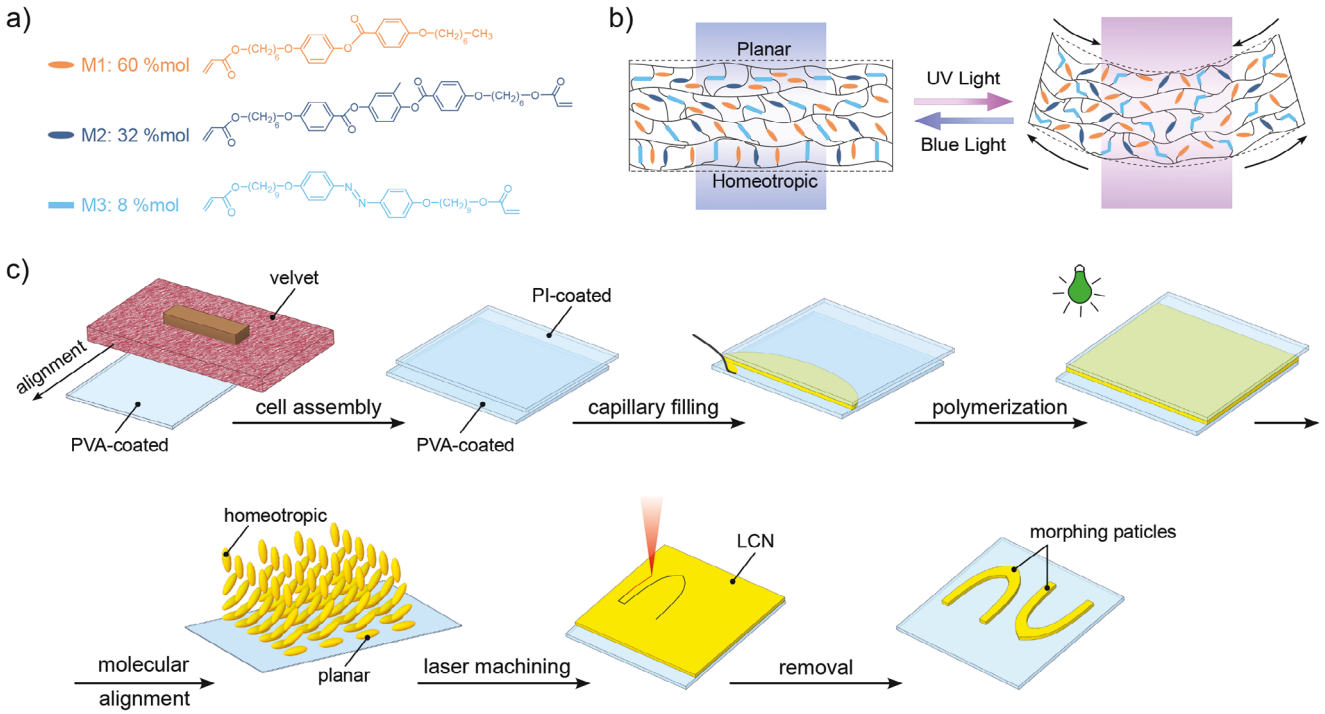

Figure 3. Liquid crystal networks. a) Molecular structure and composition of photochemical LCNs. b) Mechanism of bending actuation of photochemical LCNs undergoing *trans*-to-*cis* isomerization upon exposure to UV and *cis*-to-*trans* relaxation upon exposure to blue light. c) Schematic shows the steps taken for the fabrication of LCN chassis starting with surface-alignment of LCN precursor in capillary cells (splay-aligned), followed by polymerization using green light, and finally laser micromachining to achieve the final geometry.

resulting in uncontrolled random trajectories. In contrast, if the motor coating is applied to specific predefined locations, the localized release of fuel will generate anisotropic surface tension gradients and therefore anisotropic motion with a preferred direction (Figure 2d). This anisotropic propulsion results in long-range linear motion over the available water surface. Tracking these two types of particles and analyzing their trajectories (motion relative to the initial locomotion direction axis) highlights the difference in directionality: while isotropic particles exhibited a random distribution of directions from 0°–360° (random locomotion), anisotropic particles exhibited a constant narrow direction around 0° (linear motion) (Figure 2e). These experiments, indeed, demonstrate that the judicious application of modular protein motor coatings at predefined locations on small-scale objects can be leveraged to control the direction of motion and to engineer self-powered locomotion and navigation at the water-air interface.

2.3. Shape-Morphing Photochemical Liquid Crystal Networks

In order to fulfill the requirements of our morphing swimmer design, we synthesized and developed an acrylate-based photochemical LCN. Our formulation consists of a side-chain mesogenic mono-acrylate backbone (M1), a mesogenic diacrylate crosslinker (M2), and a photo-active mesogenic azobenzene diacrylate crosslinker (M3) (**Figure 3a**). The LCN was polymerized with Irgacure 784 as the photoinitiator using green light, rather than the standard of ultraviolet (UV) light, to ensure that the azobenzene moieties were in the *trans*-state during polymerization. The azobenzene crosslinker undergoes isomerization from the extended *trans*-isomer to the bent *cis*-isomer upon exposure to UV light and transitions back from *cis*-to-*trans* upon exposure to blue or green light (Figure 3b). LCN films were first fabricated inside capillary cells of 50 µm gap with either planar or splay alignment (Figure 3c). The alignment of LCN films was confirmed after fabrication via crossed-polarizers and also observed by SEM (Figure 2b). The films then were cut by laser micromachining into predefined form factors for the characterization and fabrication of swimmers.

To find an optimal formulation of LCN that meets all the conditions mentioned in the concept design: a) tunable chemistry with reversible and on-demand bending and relaxation, b) large strains, and c) sustained shape change in the absence of continued exposure to stimuli, we optimized the ratio between M1, M2, and M3. Five different formulations were studied, with either 6 or 8 mol% azobenzene and total crosslinking mol% ranging from 28% to 65%. For brevity, we named these compositions PX-Y, where X is the total mol% of crosslinking and Y is the mol% of azobenzene. The bending behavior of each formulation was studied through exposure to UV and blue light (**Figure 4a**; Movie S2, Supporting Information). All films made from five tested formulations displayed large shape changes upon exposure to UV light and relaxation upon exposure to blue light, i.e., meeting condition (a). While planar-aligned LCN was also capable of bending, it was found that a splay alignment resulted in greater tip displacement under the same exposure conditions, i.e., meeting condition (b). The samples were also all

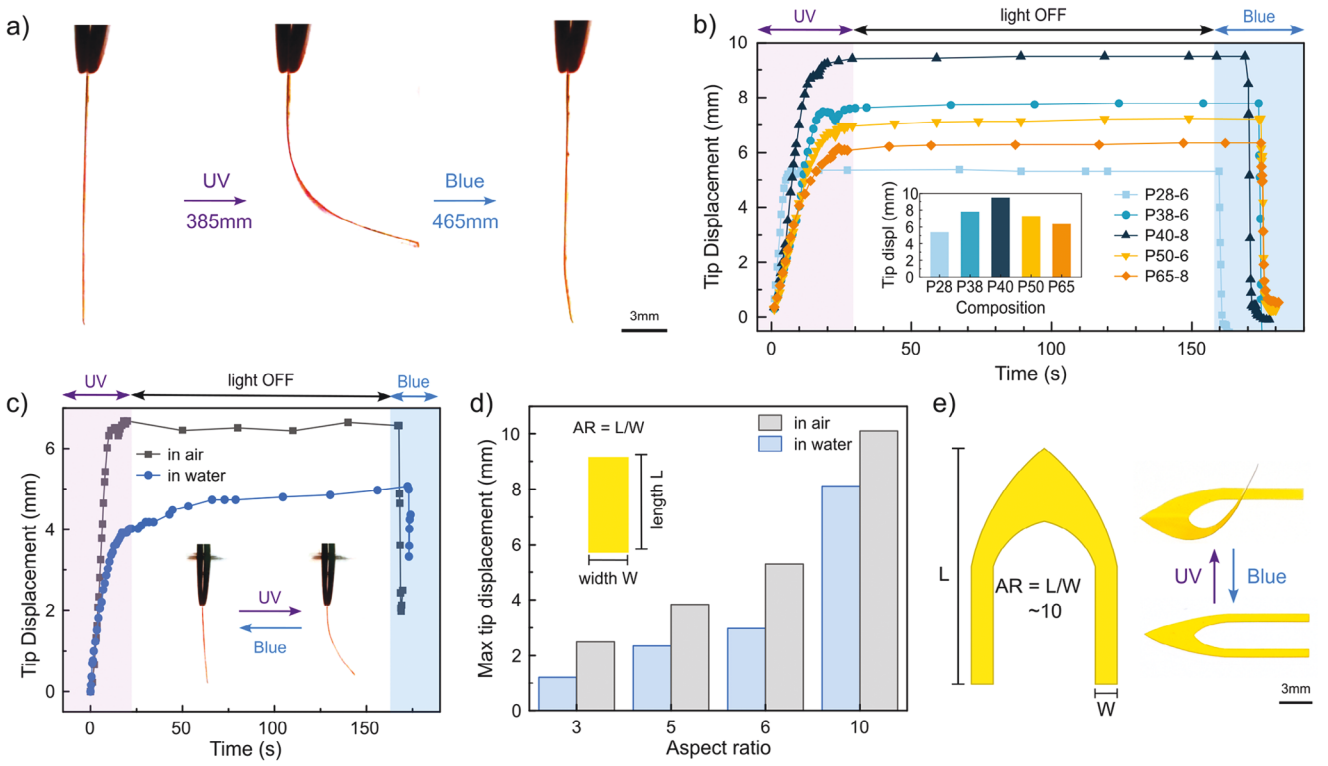

Figure 4. Actuation characterization of liquid crystal networks. a) Straight LCN cantilevers show large stable bending toward light when exposed to UV and relax back to straight geometry after being illuminated with blue light. b) Tip displacement of the cantilevers (*AR*=10) with different formulation with time. The purple region shows bending when the UV light is ON, followed by the light OFF, and finally relaxation when blue light is ON. c) Tip displacement of the cantilevers (*AR*=10) in air and water showing the large difference in the maximum bending between them. d) Variation of tip displacement under the illumination of UV with identical intensities, leading us to choose *AR*=10 as the desired geometry. e) Final micromachined geometry of LCN swimmers that shows the fidelity in selective actuation and relaxation of each leg.

able to hold the deformed shape upon ceasing exposure to UV light (for at least 2.5 min, Figure 4b). This demonstrated that the selected azobenzene crosslinker has a sufficient *cis*-lifetime to maintain shape change without continuous light exposure, i.e., meeting condition (c). Formulation P40-8 resulted in the greatest tip displacement under the same exposure conditions. Bending (measured through tip displacement) increased with increasing crosslinker content up to 40% (P40-8), after which it decreased with increasing crosslinker content. This suggests that a minimum amount of crosslinking is required to efficiently translate the disruption of order in the LCN into macroscopic shape change. However, a further increase in crosslinking beyond this threshold increases the stiffness of the material, resulting in a reduction in bending. This can also be seen in elastic modulus, with a significant increase in E when the crosslinker mol% increases from 28% to 38% (Figure S4, Supporting Information). Formulation P40-8, in addition to resulting in the greatest degree of on-demand bending, also had a suitably low 1/E, and as such was selected as the composition to use for fabricating the active swimmer.

To better understand the impact of water on the swimmer's morphing behavior, the actuation of P40-8 in air and water was examined and compared (Figure 4c, Movie S3, Supporting Information). The LCN actuation was slower and had reduced tip displacement in water compared to air. The initial slope of the linear region is lower, and the actuation of the sample takes longer to reach a plateau in water. This may be in part attributed to faster rates of heat dissipation in water than in air. Note that while the LCN bends primarily due to photochemical effects, it has been shown that the photothermal effects, even though very small, also play a part in photochemical mechanisms.[52] As such, we speculate that faster dissipation of heat in water significantly reduces the efficiency of the photothermal contribution to bending. Additionally, and perhaps more importantly, the LCN experiences greater hydrodynamic pressure when bending in water. At maximum bending speed, the LCN experiences a hydrodynamic force that is ≈160 times greater in water ($5{\cdot}10^{-5}$ Pa in water versus $3{\cdot}10^{-7}$ Pa in air), which significantly slows the speed of bending. LCNs must also overcome hydrodynamic force when bending, which reduces the maximum amount of bending achieved. Cycling tests were performed on LCN cantilevers to characterize the stability of photochemical systems over many actuation cycles (Figure S5, Supporting Information). In both air and water, the LCN maintains its ability to reach maximum tip displacement even after 10 cycles. Furthermore, we have characterized the stability of photochemical LCN actuation under different wavelengths of light (Figure S6, Supporting Information). The photochemical LCN cantilevers exhibited high stability and shape retention over a large number of cycles and under different wavelengths of light, a key advantage over photothermal systems.

Last, the effect of actuator geometry on the degree of bending was also investigated to determine the optimal form factor to

guide the design of the swimmer's legs, as the swimmer needs to overcome elastocapillary forces to deform in and out of the air-water interface. Elastocapillary length is the length scale at which capillary forces can begin to deform an elastic material. When designing a material that needs to resist capillary force, the elastocapillary force should be minimized. Elastocapillary length is proportional to the surface energy and inversely proportional to the elastic modulus of a material ($l \propto \gamma/E$). Three approaches can be taken to minimize elastocapillary effects: reducing the surface energy of the material (which can be done by surface modification), maximizing the elastic modulus of the LCN (which can conflict with bending, as previously determined), and optimizing the actuator aspect ratio above the elastocapillary length to ensure effective bending and deformation. As can be seen in Figure 4d, increasing aspect ratio (AR) results in greater bending. When placed on the surface of the water, there is a reduction in the degree of bending, however, the trend remains the same and the samples with larger AR have larger bending. As such, an aspect ratio of 10 was selected for the swimmer design to overcome the elastocapillary length and to ensure enough bending to deform in and out of the air-water interface (Figure 4e).

2.4. Design of Self-Propelled Morphing Swimmers

We integrated the protein motor and photochemical LCN into a self-propelled shape-morphing materials system to design a steerable Marangoni swimmer. The swimmer had a pointed head based on a standard G1 ballistic profile (originally designed for bullets) to adapt its low drag coefficient and reduce drag resistance in the water.[21] In addition, it had a posterior concave cavity to facilitate the accumulation of released fuel and generate anisotropic fuel concentration and surface tension gradients. The swimmer also had two posterior legs with an aspect ratio of 10 (optimized from LCN bending actuation analysis) that bend upward or downward to enable steering. This design was microfabricated from photochemical LCN films by laser micromachining (Figure S7, Supporting Information). spanning length scales from 10 to 1 mm (Figure S8a, Supporting Information). Then, the modular motor system was applied as a coating to the posterior cavity and legs of swimmers (Figure S8b, Supporting Information).

In its initial passive configuration (*mode I*) neither LCN legs have been actuated and they are resting flat, and the fuel is released in the posterior cavity, propelling the swimmer forward (**Figure 5a**). The release of fuel to the surrounding water medium was simulated in Figure 5b to observe the resulting fuel concentration profile. A concentration of 2 kmol m^{-3} embedded fuel in the protein matrix was used as an initial state at time zero, based on prior analyses of absorbed and retained HFIP in SRT proteins.[47] To simulate realistic conditions of fuel release during locomotion (i.e., diffusion from a moving source), the surrounding water has a flow at velocities and directions determined experimentally for each mode. The resulting concentration map shows an anisotropic gradient toward the back of the swimmer. Fuel concentration profiles can be directly converted to surface tension maps (linear approximation at low concentrations),[21] which in turn generate Marangoni propulsive forces. In *mode I*, the two legs and posterior cavity form a nozzle at the stern that generates a steady release of fuel in the backward direction, thus generating Marangoni forces that propel the swimmer forward. In *mode II*, one of the photochemical LCN legs is bent upward, thus separating from the air-water interface and opening the posterior cavity on one side. In this configuration, the fuel is released in the posterior cavity but also it can diffuse to one of the sides, resulting in anisotropic fuel concentration and surface tension gradients both in the bow/stern and port/starboard directions. Therefore, the generated Marangoni forces in this configuration will have both forward and lateral components that will simultaneously propel forward and rotate the swimmer. Last, in *mode III*, one of the LCN legs is bent downward and submerged in water. Similar to *mode II*, this configuration also opens the posterior cavity to allow for lateral diffusion of fuel; however, the submerged leg adds drag resistance on the bent side. Therefore, we expect this configuration to exhibit a slower propulsion with a higher rotation rate. These three configurations and simulated profiles of fuel diffusion provide a fast, linear propulsion *mode I*, a fast rotation *mode II*, and a slow rotation *mode III* that will be combined to steer the swimmer and achieve complex trajectories.

2.5. Locomotion of Self-Propelled Morphing Swimmers

The simulated design and locomotion mechanisms were implemented and experiments were conducted to validate them for a protein motor-LCN hybrid system. First, we validated the feasibility of steering control and propulsion plus rotation modes in non-morphing swimmers. We fabricated symmetric as well as asymmetric swimmer structures by removing one of the posterior legs in order to open the diffusion cavity as simulated. We analyzed the locomotion behavior of these non-morphing structures over length scales ranging from 1 to 10 mm (Movie S4, Supporting Information). In all cases, when the swimmer contacts the water surface, it will quickly accelerate and reach its maximum velocity due to the release of fuel (which will slowly decrease in time as fuel is depleted). The symmetric swimmer (similar to *mode I*) exhibited linear trajectories in all length scales (Figure S9a, Supporting Information). The asymmetric swimmers exhibited clockwise and counterclockwise trajectories for right and left diffusion cavity opening respectively (similar to *mode II*), which was consistent with the simulated behaviors (Figure S9b,c, Supporting Information). While the symmetric swimmer exhibited small deviations in trajectory (within ± 3°), asymmetric swimmers exhibited consistent curved trajectories of 50–60° rotation per body length (Figure S10a, Supporting Information). We observed that the maximum velocity decreases with characteristic length scale following a $\sim l^{-1/3}$ dependence due to a larger submerged area and, consequently, larger drag resistance as described in previously developed physical models.[47] In our design, the swimmer with the smallest characteristic length size (1 mm) reached the maximum speed of ≈160 mm s^{-1} and decreased to ≈90 mm s^{-1} for 10 mm swimmers due to increased drag resistance with larger size (Figure S10b, Supporting Information). Asymmetric

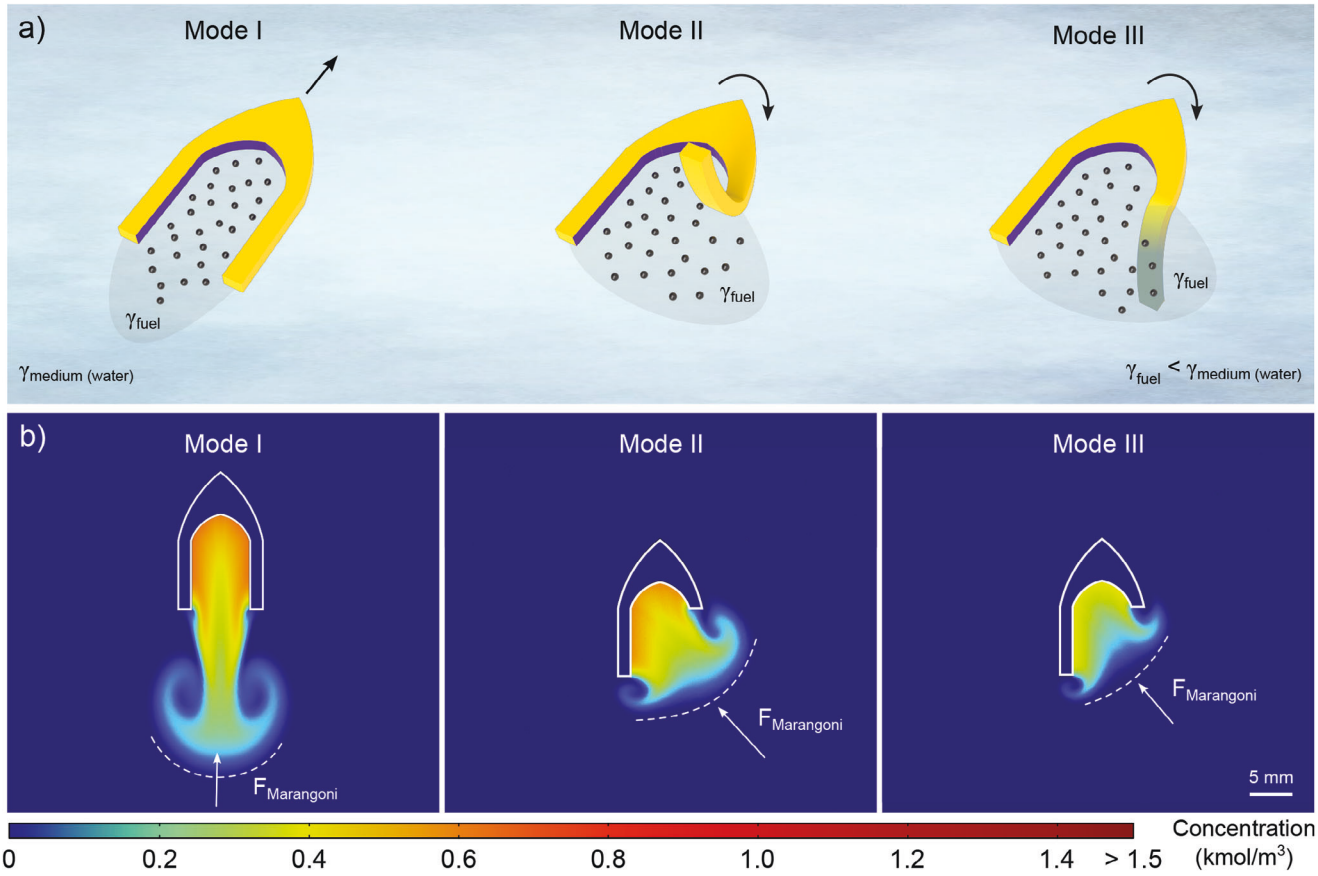

Figure 5. Design and simulation of swimming modes. a) Swimming modes as a function of morphing configuration: *mode I* - flat posterior legs, *mode II* - one leg bent upward, and *mode III* - one leg bent downward (partially submerged). b) Simulation of released chemical fuel concentration maps for each swimming mode and corresponding morphing configuration.

swimmers showed a similar trend with length scale dependence and showed a slightly lower speed due to increased drag resistance (the cross-sectional area exposed against flow is larger when rotating). These swimmers mainly consist of an LCN chassis with only a thin film of fuel-infused protein as a modular propulsion source, yet, the generated Marangoni forces are enough to propel them at high velocities. The efficiency of this motor system is calculated as the kinetic energy of the swimmer (that depends on speed and the total mass of the swimmer) per unit mass of fuel. Considering the high speeds reported and the small amount of fuel (3–40 µg), we calculated efficiencies of 153, 163, 337, 347 µJ g^{-1} for 1 to 10 mm length scale swimmers (Figure S11, Supporting Information). The efficiency of this motor system applied to LCNs greatly surpasses those reported for other Marangoni systems and other families of micromotors.[21] Through these asymmetric swimmers, we could validate *mode I* and *mode II* locomotion in non-morphing structures, demonstrating the feasibility of achieving linear versus curved trajectories through swimmer design and modulation of the fuel diffusion cavity. However, these non-morphing structures can only perform one locomotion mode.

Next, we implemented these designs in a shape-morphing photochemical LCN chassis capable of transitioning between locomotion modes and directions in a single structure. LCN cantilever actuators were integrated as the swimmer's posterior legs that can bend under UV light and release the deformation back to their original flat shape under blue light. From this, we obtained a recoverable deformation of the posterior leg with a maximum tip displacement of 8.7 mm. To overcome the capillary force generated by the water surface to flatten the sample, we functionalized the surface of the legs with fluorosilane to reduce their surface energy and increase their hydrophobicity. The contact angle between LCN films and water increased from 68° to 91° after silanization (Figure S12, Supporting Information), and, as a result, the stability of the actuated cantilever leg on the air-water surface was largely extended (Movie S5, Supporting Information). By selectively actuating the swimmer's posterior legs to bend upward or downward from the water surface, we can obtain five different locomotion modes based on the previously simulated designs (**Figure 6**a; Movie S6, Supporting Information). First, for flat swimmers (*mode I*), the fuel concentration released by the protein motor coating in the posterior cavity is symmetrical about the center of the entire swimmer structure. Therefore, the resulting Marangoni driving force that acts on the swimmer's center of mass points straight ahead, producing a forward linear motion trajectory. Then, while the swimmer's leg is bent upward away from water, *mode II_L* and *mode II_R* were achieved (L and R denote which leg is actuated), the release of HFIP fuel in the

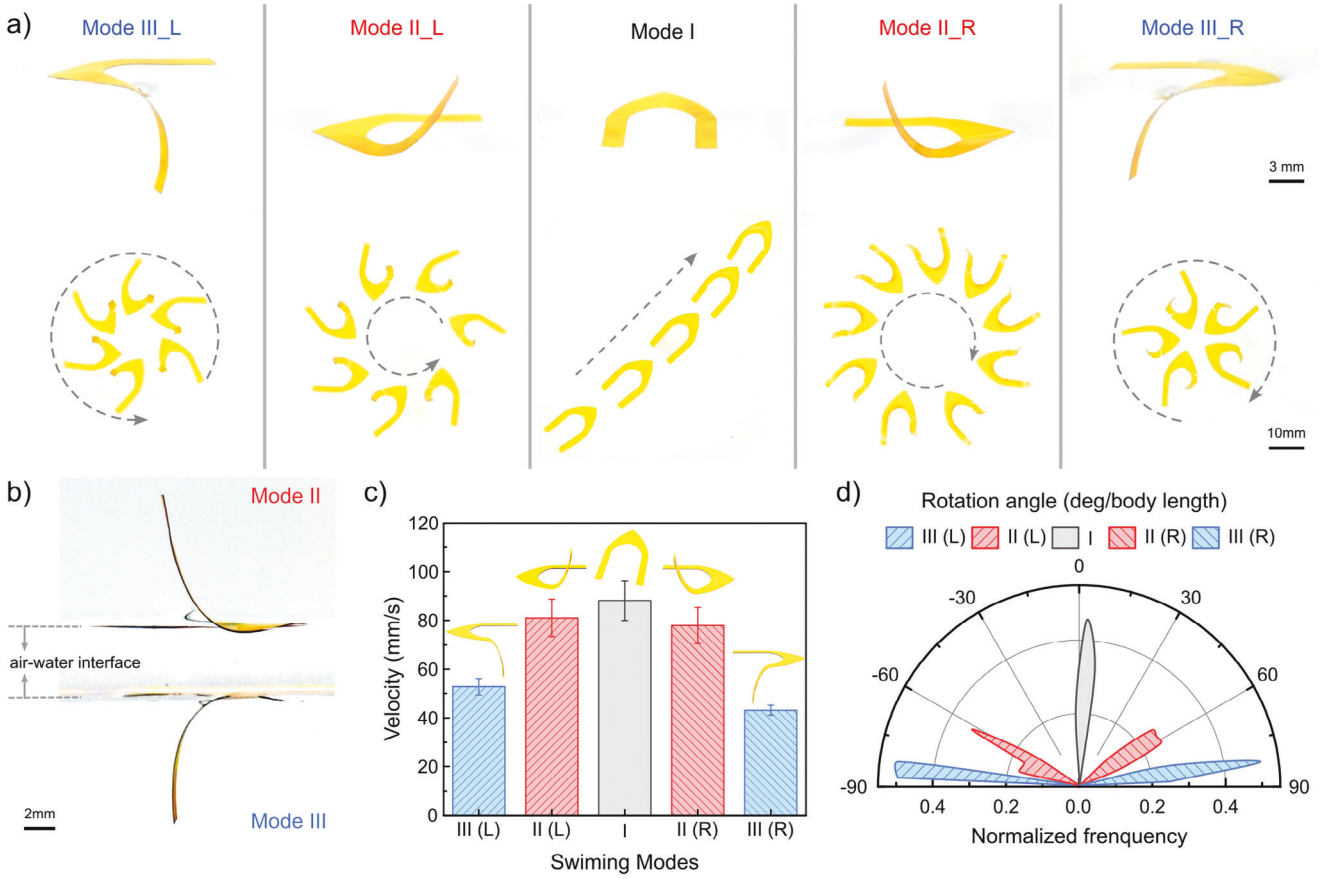

Figure 6. Locomotion of shape-morphing swimmers. a) Swimmer morphing configurations and corresponding locomotion modes as a function of posterior leg bending upward or downward from water surface. b) Side view of swimmers standing on water surface under *mode II* and *mode III*. c) Maximum speed and d) body rotation angles of swimmers when varying locomotion modes.

posterior cavity is asymmetric and produces a lateral component of the surface tension gradient and resulting Marangoni force. The resulting force drives the swimmer to rotate toward the side without bending deformation and opening. Last, one leg of the swimmer is bent downward below the water surface (*mode III_L* and *mode III_R*). Due to the lateral opening of the diffusion cavity, the asymmetric surface tension gradient generates a Marangoni force with a lateral component that induces rotation in addition to propulsion (similar to *mode II*). In *mode I*, the swimmer moves in a straight direction, with a minimal area exposed against the flow resulting in an optimized drag resistance. As the swimmer starts rotating in *mode II* and in *mode III*, a larger surface is exposed against the flow, thus increasing drag. Furthermore, the actuated leg configuration can be clearly observed in Figure 6b: while in *mode II* the leg bends upward and slightly deforms the free surface of water (observable as a meniscus under the leg), the actuated leg is completely submerged in *mode III*. The submerged leg results in further increased drag resistance due to a larger surface of solid body moving against flow. The increased drag in *mode II* and *mode III* from rotation and submerged body respectively result in slower locomotion speeds compared to *mode I*, with speeds of 90, 80, and 45 mm s^{-1} for *mode I*, *II*, and *III* respectively for 10 mm swimmers (Figure 6c). *Mode I* exhibits long-range linear stable trajectories, however, *mode II* exhibits curved trajectories with a rotation of ~60° per body length (Figure 6d), agreeing with the previous speed and trajectory rotation of non-morphing swimmers. Mode III exhibits a large rotation of ~85° per body length, resulting in close curvature orbiting trajectories. Because the increased drag arising from the submerged leg is applied to either side of the center of mass, *mode III* results in a higher torque and a larger rotation than *mode II*. Both *mode II* and *III* configurations had the same speed but opposite rotation and trajectories depending on which left or right leg was actuated. Therefore, these reported shape-morphing and swimmer leg actuation mechanisms give access to five distinct modes of locomotion within a single swimmer by modulating the fuel release cavity and drag distribution. These modes include a standard linear propulsion mode plus two types of rotation in each direction, thus enabling programmable steering capabilities for the control of the swimmer.

2.6. Dynamic Active Transition of Swimming Modes Via Shape-Morphing

The use of photoresponsive chassis structures not only enables a variety of swimming modes but also provides a method for actively transitioning between them and controlling the trajectory

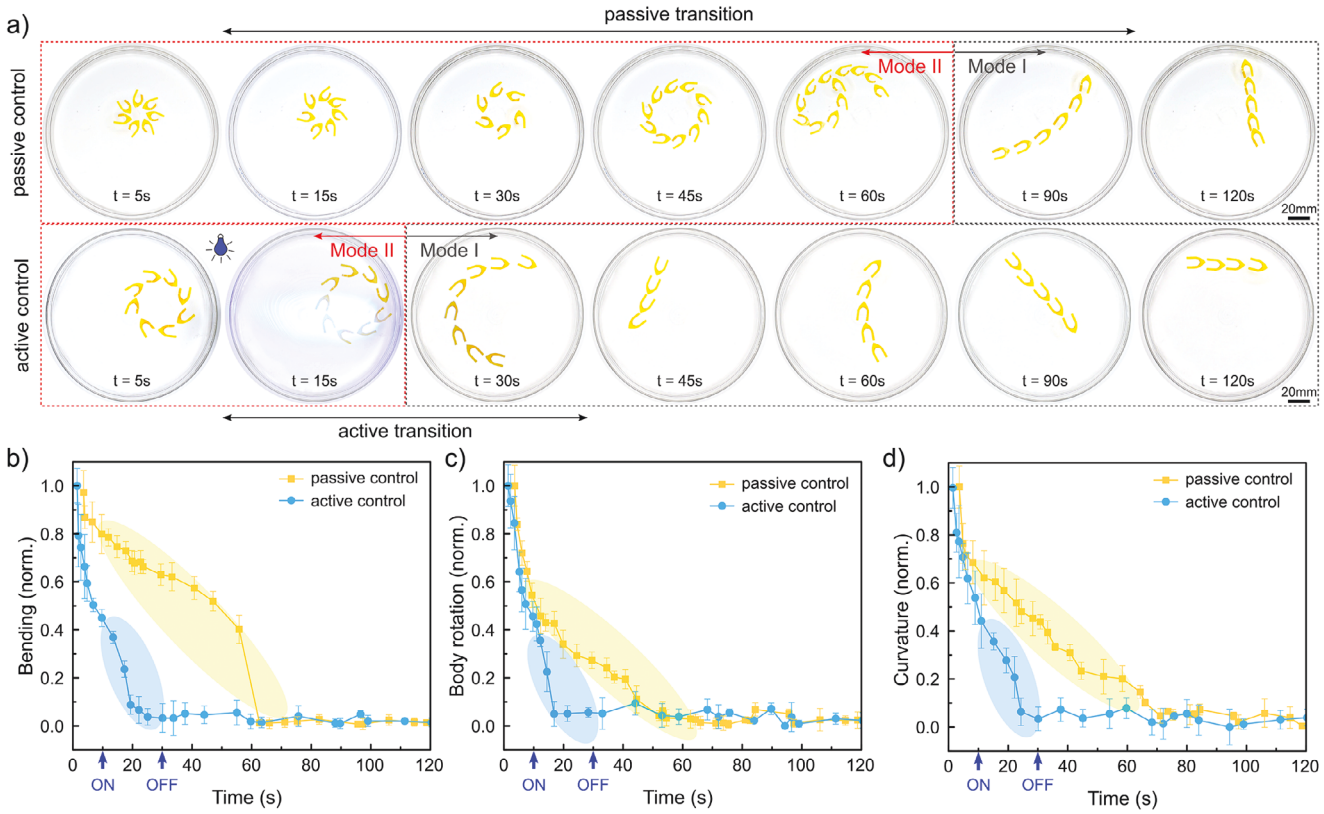

Figure 7. Trajectory transitions. a) Transition progresses from swimming Mode II (rotation) to swimming Mode I (linear movement): passive transitions happen under the capillary force between 10 and 90 s, and active transitions happen under blue light between 10 and 30 s. b–d) Characterization of transition progresses through the normalized b) bending of swimmers' legs, c) rotation of swimmers' bodies, and d) curvature of trajectories in both passive control and active control scenarios.

and locomotion via steering. Leveraging the programmed actuation of the LCN structures to bend in and out of the water surface plane, here we analyze the transition from *mode II* to *mode I* to demonstrate control capabilities. For example, in *mode II*, the leg is actuated and bent upward. In this configuration, the deformed cantilever creates an upward meniscus that pulls down and gradually relaxes the leg over time. This relaxation of the leg can be leveraged to design a passive transition from bent to flat over time. As the bent leg flattens over time, the diffusion cavity opening is slowly closed toward a symmetric *mode I* configuration, thus eliminating the rotation and transition from curved to linear trajectory (**Figure** 7a).

In a passive mode transition scenario, the swimmer sustained *mode II* swimming for ≈90 s, after which *mode I* of swimming dominated (Movie S7, Supporting Information). While effective, this passive transition is slow and does not provide a fast switching for on-demand trajectory control. In contrast, light was used to trigger the relaxation of the bent leg on demand and accelerate the transition. We induced dynamic active transitions between these two modes by exposing the swimmer to the blue light, which triggered a rapid relaxation of the bent leg due to photochemical *cis*-to-*trans* isomerization. Under light-fueled actuation, the active transition takes <10 s of global illumination time to switch from *mode II* to *mode I* locomotion (note that the actual time the swimmer is exposed to light is much smaller). The difference between passive and active locomotion mode transitions is observed in Figure 7b–d, which shows the variation of bending deformation, rotation angle, and the curvature of the trajectory with time. While the passive control of the transition equilibrates well after 1 min, the active control transition takes <10 s of illumination to achieve the same locomotion mode switching. This active control strategy provides better control over the trajectory on demand and can be extended to other locomotion modes as needed (for example, *mode III* to *mode* I, Movie S8, Supporting Information).

3. Conclusion

Through the integration of chemical motors and light-responsive materials, we demonstrated strategies to provide untethered power and control, respectively, for milli-scale swimming robots. This propulsion and steering approach is inspired by semiaquatic insects that release biosurfactants to generate Marangoni flow and deform the free surface of the water to manipulate the meniscus to steer. Here, we used a Marangoni motor system based on structural protein with a self-regulated porosity releasing a low surface tension chemical fuel as a modular propulsion source. In parallel, we have developed a photo-responsive liquid crystal network for the active chassis structure to bend away from the water surface plane and deform the free surface. The integration of these two responsive materials systems has enabled the fast, efficient, long-lived propulsion of milli-scale swimmers as

well as the shape-morphing of the chassis to modulate the spatial release of fuel and steer the swimmer. The combination of these two mechanisms gives access to five different modes of locomotion in a single swimmer including linear motion, steering in two directions with the legs bent above the water surface, and steering in two directions with the legs submerged underwater (which also modulates the drag resistance to achieve smaller curvature steering). Furthermore, we demonstrate transitioning between these locomotion modes either via passive control (harnessing programmable deformation and recoverable relaxation over time) or active control (triggering shape-morphing with external light stimuli on demand) for slow/fast steering. While certain aspects can be further optimized for a more specific on-demand actuation toward pre-defined robotic tasks and performance (for example, flood versus spot illumination, closed-loop feedback, modes of swimming, etc.), the novel approach presented here has a threefold significant contribution to the soft robotics and responsive materials fields: i) it demonstrates the bioinspired integration of responsive materials to successfully mimic the swimming and control mechanisms of water treader and similar semiaquatic insects, ii) it provides a new materials-based solution to shape-morphing in water, thus overcoming limitations of actuation due to energy dissipation and surface tension by designing photochemical LCNs, and iii) it successfully implements the bioinspired concept in a small-scale functional swimming robot with untethered and orthogonal power, actuation, and steering capabilities.

4. Experimental Section

Materials: Mono-functional monomer 4-(6-acryloxy-hex-1-yl-oxy)-phenyl 4-(hexyloxy)-benzoate (M1), bi-functional monomer 1,4-bis-[4-(6-acryloyloxyhexyloxy) benzoyloxy]−2-methylbenzene (M2), and photo-active bi-functional azobenzene monomer 4,4′-Bis[9-(acryloyloxy)nonyloxy]azobenzene (M3) were purchased from SYNTHON Chemicals GmbH & Co. KPG. Bis(2,6-difluoro-3-(1-hydropyrrol-1-yl)phenyl)titanocene (Irgacure 784), polyvinyl alcohol, N,N-dimethylformamide (DMF), 1,1,1,3,3,3-hexafluoro-2-propanol (HFIP), crystal violet dye, and trichloro(1H,1H,2H,2H-perfluorooctyl)silane were purchased from Sigma–Aldrich. Polyimide SE-5661 was donated by Nissan Chemical Industries. All regents and solvents were used as received without further purification. SRT proteins were extracted from the tentacles of the *Loligo vulgaris* squid species from Tarragona (Spain).

Fabrication of Protein Motor System: SRT were isolated from squids and purified as described elsewhere.[53] SRT proteins were dissolved in HFIP at a concentration of 50 mg mL^{-1} and left to rest overnight. The protein solution was then cast on a substrate (either directly drop cast, spread with a brush, or cast on a stencil mask) to cover the desired surface, and was left for 3 h to evaporate. Disk particles were coated either on the full circumference (isotropic) or on a single spot (anisotropic), and morphing swimmers were coated on the inner cavity of the legs.

Synthesis and Fabrication of LCN: LCN films were synthesized inside capillary cells with a 50 µm gap. The cell had a pre-determined molecular alignment, homeotropic on one side and planar on the other, achieved through spin-coating. A mixture of M1, M2, and M3 monomers was melted and injected into the cell at 115 °C (above the mixture's clearing point, T_{NI}). The cell was cooled to below T_{NI} and then cross-linked using photo-polymerization through exposure to green light. LCN films were surface treated via ozone cleaning followed by exposure to trichloro(1H,1H,2H,2H-perfluorooctyl)silane in a vacuum chamber for 12 h. Round disk-shaped LCN particles were fabricated by cutting pristine LCN films using an EMS-Core sampling tool with a diameter of 4 mm. Bullet-shaped swimmers were fabricated from LCN films by laser micromachining using a 25 W Universal Laser Systems CO_2 laser cutter (5% power, 10% speed, 1000 ppi, 1.5″ optics) following the specified CAD model and length scale.

Simulation of Fuel Release: COMSOL was used to simulate fuel release of different shape-morphing modes after 100 ms. The initial embedded fuel concentration within the protein solid structure was $c = 2$ kmol m^{-3}, the diffusion coefficient of HFIP in water $D_{medium} = 3.2{\cdot}10^{-9}$ m^2 s^{-1}, and the diffusion coefficient of HFIP in the protein $D_{internal} = 7.25{\cdot}10^{-10}$ m^2 s^{-1}, according to previously reported work.[21] The flow speed and direction were set according to experiment-validated initial values.

Materials Characterization: The alignment of synthesized LCNs was confirmed using a crossed-polarizer. The structure of LCNs and protein motors were analyzed by Fourier Transform Infrared (FTIR) spectroscopy in a ThermoFisher Nicolet iS20 spectrometer with an Attenuated Total Reflection (ATR) accessory at 128 scans and 4 cm^{-1} resolution per spectrum. The resulting FTIR spectra were baseline-corrected and normalized to the Amide I band. Scanning electron microscopy (SEM) was used to characterize the interfacial morphology of LCN particles and protein motor coatings. Samples were coated with a gold film (10–20 nm) in a SPI-Module Sputter Coater and imaged on the Thermo Fisher Nova 200 Nanolab scanning electron microscope. Mechanical tensile testing using a CellScale Univert tensile machine with a load cell of 10N was used to determine elastic modulus. Contact angles of DI water on LCN films were measured using a Ramé-Hart 200-F1 goniometer to determine the wettability.

LCN Actuator Characterization: Splay-aligned cantilevers of different aspect ratios were used to study the photochemical behavior of the LCNs. The cantilevers were fixed at one end and exposed to light from a Lumen Dynamics X-Cite XLED source to determine their bending behavior. The wavelengths and intensities of the lights used in the experiments are as follows: Red (635 nm, 0.1 W cm^{-2}), Green (565 nm, 0.14 W cm^{-2}), Blue (460 nm, 0.11 W cm^{-2}), UV (385 nm, 0.05 W cm^{-2}). The bending behavior was characterized by measuring the tip displacement and bending angle using a Dino-lite digital microscope. Cycling tests in either air or water were performed by repeatedly irradiating a 1.5 × 10 mm LCN cantilever with the following light cycle 10 times: UV light on for 15 s, lights off for 15 s, blue light on for 15 s. Color tests were performed by irradiating the cantilever in 15-s intervals in the following patterns: red, green, blue, UV, red, green, blue.

Modular Motor Coating and Motor Performance Analysis: The protein motor solution was applied to the posterior legs of swimmers. Coated swimmers were transferred to petri dishes with DI water and their locomotion was recorded with a Nikon D3500 camera. Morphing swimmers were actuated using broad flood illumination from an OmniCure S1500 UV Curing System with a UV filter (320–390 nm, 0.48 W cm^{-2}) and a blue light filter (400–500 nm, 0.17 W cm^{-2}). Tracker software was used to obtain coordinates of the mass center, symmetric axis, and deformed tip of swimmers. MATLAB was used to generate swimmers' locomotion map and calculate the locomotion speed (mass center moving speed along trajectory lines), bending (projection of tip displacement on symmetric axis), body rotation (swimmers' symmetric axis rotating around the trajectory tangent), and trajectory curvature (trajectory tangent).

Supporting Information

Supporting Information is available from the Wiley Online Library or from the author.

Acknowledgements

C.H. and A.P.F. acknowledge the National Science Foundation – Materials Research Science and Engineering Center at the University of Michigan (Award No. DMR-2309029) for partial support of this research. H.S. acknowledges the Natural Sciences and Engineering Research Council of Canada (NSERC). The authors acknowledge the University of Michigan College of Engineering for financial support and the Michigan Center for Materials Characterization for the use of the instruments and staff assistance.

Conflict of Interest

The authors declare no conflict of interest.

Author Contributions

C.H. and N.P.P. contributed equally to this work. H.S. and A.P.F. conceived, designed, and supervised the research. C.H. fabricated the morphing swimmers, characterized the chemical motor system, and performed all swimming experiments, simulations, and analyses. N.P. synthesized and characterized the LCNs and optimized their photochemical behavior. C.H.L. performed initial tests on non-morphing swimmers. I.H.T. and M.S. performed LCN cycling tests. All authors participated in manuscript revisions, discussions, and interpretation of the data.

Data Availability Statement

The data that support the findings of this study are available in the supplementary material of this article.

Keywords

liquid crystal network, marangoni, microrobot, photochemical, shape-morphing, surface tension

Received: July 22, 2024
Revised: September 4, 2024
Published online: October 1, 2024

[1] U. Bozuyuk, P. Wrede, E. Yildiz, M. Sitti, *Adv. Mater.* **2024**, *36*, 2311462.
[2] J. Li, B. Esteban-Fernández de Ávila, W. Gao, L. Zhang, J. Wang, *Sci. Robot.* **2017**, *2*, eaam6431.
[3] V. Iacovacci, E. Diller, D. Ahmed, A. Menciassi, *Annu Rev Biomed Eng* **2024**, *26*, 561.
[4] M. Li, A. Pal, A. Aghakhani, A. Pena-Francesch, M. Sitti, *Nat. Rev. Mater.* **2022**, *7*, 235.
[5] X. Z. Chen, B. Jang, D. Ahmed, C. Hu, C. De Marco, M. Hoop, F. Mushtaq, B. J. Nelson, S. Pané, *Adv. Mater.* **2018**, *30*, 1705061.
[6] S. Tottori, L. Zhang, F. Qiu, K. K. Krawczyk, A. Franco-Obregón, B. J. Nelson, *Adv. Mater.* **2012**, *24*, 811.
[7] K. E. Peyer, S. Tottori, F. Qiu, L. Zhang, B. J. Nelson, *Chemistry* **2013**, *19*, 28.
[8] H. Shahsavan, A. Aghakhani, H. Zeng, Y. Guo, Z. S. Davidson, A. Priimagi, M. Sitti, *Proc. Natl. Acad. Sci. USA* **2020**, *117*, 5125.
[9] D. Han, Y. Zhang, J. Ma, Y. Liu, B. Han, H. Sun, *Adv. Mater.* **2016**, *28*, 8328.
[10] A. Aghakhani, A. Pena-Francesch, U. Bozuyuk, H. Cetin, P. Wrede, M. Sitti, *Sci. Adv.* **2022**, *8*, eabm5126.
[11] D. Ahmed, T. Baasch, B. Jang, S. Pane, J. Dual, B. J. Nelson, *Nano Lett.* **2016**, *16*, 4968.
[12] Y. Alapan, B. Yigit, O. Beker, A. F. Demirörs, M. Sitti, *Nat. Mater.* **2019**, *18*, 1244.
[13] J. G. S. Moo, M. Pumera, *Chemistry* **2015**, *21*, 58.
[14] X. Ma, A. C. Hortelão, T. Patiño, S. Sánchez, *ACS Nano* **2016**, *10*, 9111.
[15] K. K. Dey, X. Zhao, B. M. Tansi, W. J. Méndez-Ortiz, U. M. Córdova-Figueroa, R. Golestanian, A. Sen, *Nano Lett.* **2015**, *15*, 8311.
[16] P. Cabanach, A. Pena-Francesch, D. Sheehan, U. Bozuyuk, O. Yasa, S. Borros, M. Sitti, *Adv. Mater.* **2020**, *32*, 2003013.
[17] U. Bozuyuk, Y. Alapan, A. Aghakhani, M. Yunusa, M. Sitti, *Proc. Natl. Acad. Sci. USA* **2021**, *118*, 2022090118.
[18] W. Wang, W. Duan, S. Ahmed, T. E. Mallouk, A. Sen, *Nano Today* **2013**, *8*, 531.
[19] J. Plutnar, M. Pumera, *Angew Chem, Int Ed* **2019**, *58*, 2190.
[20] A. Aghakhani, O. Yasa, P. Wrede, M. Sitti, *Proc. Natl. Acad. Sci. USA* **2020**, *117*, 3469.
[21] A. Pena-Francesch, J. Giltinan, M. Sitti, *Nat. Commun.* **2019**, *10*, 3188.
[22] J. W. M. Bush, D. L. Hu, *Annu Rev Fluid Mech.* **2006**, *38*, 339.
[23] R. D. Allen, N. S. Allen, *Annu. Rev. Biophys. Bioeng.* **1978**, *7*, 469.
[24] J. Gray, H. W. Lissmann, *J. Exp. Biol.* **1964**, *41*, 135.
[25] D. L. Hu, J. W. M. Bush, *J. Fluid Mech.* **2010**, *644*, 5.
[26] D. L. Hu, J. W. M. Bush, *Nature* **2005**, *437*, 733.
[27] D. L. Hu, B. Chan, J. W. M. Bush, *Nature* **2003**, *424*, 663.
[28] K. E. Linsenmair, R. Jander, *Naturwissenschaften* **1963**, *50*, 231.
[29] J. W. M. Bush, D. L. Hu, M. Prakash, in *Advances in Insect Physiology*, Elsevier, Amsterdam, Netherlands **2007**, p. 117–192.
[30] W. Hu, G. Z. Lum, M. Mastrangeli, M. Sitti, *Nature* **2018**, *554*, 81.
[31] M. K. Abdelrahman, R. J. Wagner, M. S. Kalairaj, M. Zadan, M. H. Kim, L. K. Jang, S. Wang, M. Javed, A. Dana, K. A. Singh, S. E. Hargett, A. K. Gaharwar, C. Majidi, F. J. Vernerey, T. H. Ware, *Nat. Mater.* **2024**, *23*, 281.
[32] J. S. Koh, E. Yang, G. P. Jung, S. P. Jung, J. H. Son, S. I. Lee, P. G. Jablonski, R. J. Wood, H. Y. Kim, K. J. Cho, *Science* **2015**, *349*, 517.
[33] L. Zhang, J. J. Abbott, L. Dong, B. E. Kratochvil, D. Bell, B. J. Nelson, *Appl. Phys. Lett.* **2009**, *94*, 064107.
[34] P. Sartori, R. S. Yadav, J. Del Barrio, A. DeSimone, C. Sánchez-Somolinos, *Adv. Sci.* **2024**, *11*, 2308561.
[35] A. Barbot, F. Ortiz, A. Bolopion, M. Gauthier, P. Lambert, *Annu. Rev. Control Robot. Auton. Syst.* **2023**, *6*, 313.
[36] B. Kwak, J. Bae, *Bioinspir. Biomim.* **2018**, *13*, 041002.
[37] Z. Zhou, R. Mittal, *Bioinspir. Biomim.* **2017**, *13*, 015001.
[38] M. Camacho-Lopez, H. Finkelmann, P. Palffy-Muhoray, M. Shelley, *Nat. Mater.* **2004**, *3*, 307.
[39] X. Yang, Y. Chen, X. Zhang, P. Xue, P. Lv, Y. Yang, L. Wang, W. Feng, *Nano Today* **2022**, *43*, 101419.
[40] M. Pilz Da Cunha, H. S. Kandail, J. M. J. Den Toonder, A. P. H. J. Schenning, *Proc. Natl. Acad. Sci. USA* **2020**, *117*, 17571.
[41] A. H. Gelebart, D. J. Mulder, M. Varga, A. Konya, G. Vantomme, E. W. Meijer, R. L. B. Selinger, D. J. Broer, *Nature* **2017**, *546*, 632.
[42] Z. Hu, W. Fang, Q. Li, X. Q. Feng, J. Lv, *Nat. Commun.* **2020**, *11*, 5780.
[43] S. Ma, X. Li, S. Huang, J. Hu, H. Yu, *Angew. Chem, Int. Ed.* **2019**, *58*, 2655.
[44] N. P. Pinchin, H. Guo, H. Meteling, Z. Deng, A. Priimagi, H. Shahsavan, *Adv. Mater.* **2024**, *36*, 2303740.
[45] M. Helft, Z. Zhang, C. Kinane, N. Black, A. Pena-Francesch, *Integr. Comp. Biol.* **2024**, *64*, icae005.
[46] A. Pena-Francesch, H. Jung, M. Tyagi, M. C. Demirel, *Biomacromolecules* **2022**, *23*, 3165.
[47] C. H. Lin, C. Kinane, Z. Zhang, A. Pena-Francesch, *ACS Appl. Mater Interfaces* **2022**, *14*, 39332.
[48] N. P. Pinchin, C. H. Lin, C. A. Kinane, N. Yamada, A. Pena-Francesch, H. Shahsavan, *Soft Matter* **2022**, *18*, 8063.
[49] A. Pena-Francesch, H. Jung, M. C. Demirel, M. Sitti, *Nat. Mater.* **2020**, *19*, 1230.
[50] Z. Zhang, J. T. Heron, A. Pena-Francesch, *Adv. Funct. Mater.* **2023**, *33*, 2215248.
[51] I. Colomer, A. E. R. Chamberlain, M. B. Haughey, T. J. Donohoe, *Nat. Rev. Chem* **2017**, *1*, 0088.
[52] M. P. D. Cunha, E. A. J. Van Thoor, M. G. Debije, D. J. Broer, A. P. H. J. Schenning, *J. Mater. Chem C* **2019**, *7*, 13502.
[53] A. Pena-Francesch, S. Florez, H. Jung, A. Sebastian, I. Albert, W. Curtis, M. C. Demirel, *Adv. Funct. Mater.* **2014**, *24*, 7401.